Quantitative imaging through a spectrograph. 1. Principles and theory

René Tolboom, Nico Dam, Hans ter Meulen, Joris Mooij, and Hans Maassen

Laser-based optical diagnostics, such as planar laser-induced fluorescence and, especially, Raman imaging, often require selective spectral filtering. We advocate the use of an imaging spectrograph with a broad entrance slit as a spectral filter for two-dimensional imaging. A spectrograph in this mode of operation produces output that is a convolution of the spatial and spectral information that is present in the incident light. We describe an analytical deconvolution procedure, based on Bayesian statistics, that retrieves the spatial information while it avoids excessive noise blowup. The method permits direct imaging through a spectrograph, even under broadband illumination. We introduce the formalism and discuss the underlying assumptions. The performance of the procedure is demonstrated on an artificial but pathological example. In a companion paper [Appl. Opt. **43,** 5682–5690 (2004)] the method is applied to the practical case of fuel equivalence ratio Raman imaging in a combustible methane–air mixture.

OCIS codes: 000.2170, 100.1830, 100.3020.

1. Introduction

Optical techniques find increasingly more applications in (reactive or nonreactive) gas flow diagnostics.[1–3] There is good reason for that. Light-scattering techniques are as near as one can get to nonintrusive diagnostics. There are widely available (laser) light sources of unsurpassed spectral brightness that permit specific detection of selected chemical species (of great importance especially in combustion), and a large variety of experimental techniques has been developed for many specific purposes. In this paper we focus on two-dimensional (2-D) optical imaging of density distributions of specific chemical species. There are two methods of choice for this purpose,[1,2] i.e., planar laser-induced fluorescence and planar Raman scattering. Both combine a thin (quasi-monochromatic) sheet of light derived from a powerful laser system with (intensified) CCD cameras for detection of the scattered light. Both also usually require good spectral filtering of the scattered light for suppression of undesired contributions to the measured light intensity. In this paper we discuss the use of an imaging grating spectrograph with a CCD camera on the exit port [an optical multichannel analyzer (OMA)] for spectrally selective 2-D imaging. Although we have the specific purpose of Raman imaging in mind, the technique is not restricted to that and can be used for spectrally selective imaging in general. The use of a spectrograph has two main advantages over the use of spectral bandpass filters: Its spectral selectivity is greater, and it provides a spectrum. Thus undesired spectral contributions will be suppressed more effectively, and, even if unexpected spectral interferences occur, a spectrograph will at least show them, whereas they are likely to pass unnoticed when bandpass filters are used.

An ideal imaging grating spectrograph projects a faithful image of its entrance slit onto its exit plane. Where exactly on the exit plane this image ends up also depends on the wavelength of the incident light, as follows directly from the familiar grating equation[4,5] (see Fig. 1)

$$d(\sin \alpha \pm \sin \beta) = m\lambda, \tag{1}$$

where m is the order of diffraction and d is the groove center distance. Both the angles of incidence (α) and of reflection (β) are defined with respect to the grating normal (dashed–dotted lines). The + applies when α and β are on the same side of

All the authors are with Radboud University of Nijmegen, Toernooiveld 1, NL-6525 ED Nijmegen, The Netherlands. R. A. L. Tolboom, N. J. Dam (nicod@science.ru.nl), and J. J. ter Meulen are with the Department of Applied Physics and J. M. Mooij and J. D. M. Maassen are with the Mathematical Institute.

Received 24 December 2003; revised manuscript received 12 July 2004; accepted 27 July 2004.

0003-6935/04/305669-13$15.00/0

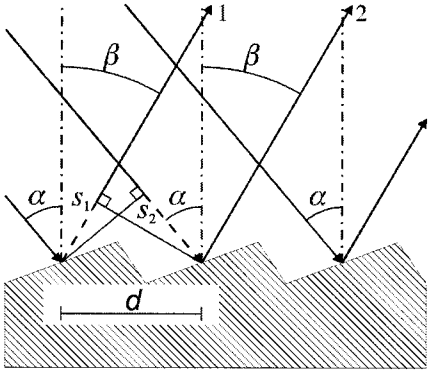

Fig. 1. Schematic representation of the diffraction of light by a grating.

the grating normal; the −, when they are on opposite sides (as in the example depicted). In most cases a spectrograph is used with a narrow entrance slit to record line (one-dimensional) spectra, e.g., Raman spectra in combustion science[1,6–9] and point (zero-dimensional) spectra for increased signal-to-noise ratios.[10,11] In the former case (one dimension), one of the axes that span the exit plane carries a spectral scale and the other one still carries purely spatial information (along the height of the entrance slit). One way to visualize planar (2-D) patterns with one-dimensional imaging is to perform consecutive line measurements for many longitudinal positions. Recently Sijtsema *et al.*[12] introduced direct 2-D imaging through a spectrograph as a nonintrusive tool for quantitative, planar gas flow visualization. This technique, referred to henceforth as OMA imaging, is the focus of the present paper. It is shown that OMA imaging, originally introduced for use with quasi-monochromatic light,[12] can be used for extended spectral structures as well.[13]

Below, we concentrate on theoretical issues related to spectrally selective 2-D imaging, using a setup that incorporates an imaging spectrograph with a diffraction grating operated in first order. The grating effectively produces an output image on the spectrograph's exit plane in which the spectral and spatial information that is present in the incident light is scrambled. It is shown that, in spite of diffraction, the original (spatial) image can nevertheless be reconstructed for many practical situations. In Section 2 we deal with the formalism that describes the scrambling of the spatial and spectral information by the imaging spectrograph. Under not-too-stringent restrictions this scrambling is shown to take the form of a convolution. Section 3 describes the straightforward analytical deconvolution that, given the spectral composition of the input, should in principle return the spatial information. This scheme, however, is shown to suffer in practice from excessive noise blowup. Therefore a linear Bayesian deconvolution filter was developed. This filter, which can still be described analytically, is presented in Subsection 3.B together with a discussion of its performance and of the way in which it is tuned to a particular application. The procedures are illustrated in this paper by means of actual recordings of a square grid that is illuminated by bichromatic light. This grid provides a fairly pathological example of the application of this algorithm, because the original object contains sharp contrast. Any algorithm that provides satisfactory results in this case may therefore be expected to perform well in less demanding cases also.

The mathematics in this paper is not exhaustive; more mathematical detail and the properties of the Bayesian filter can be found in the thesis of Tolboom.[14] A companion paper[15] (referred hereafter to as paper T2) is devoted to the practical application of the general OMA imaging results derived here to 2-D Raman imaging for fuel equivalence ratio mapping. It turns out that 2-D OMA imaging takes full advantage of an imaging spectrograph and provides a technique that is time and cost efficient for simultaneous mapping of molecule-specific 2-D density distributions.

2. Convolution by a Spectrograph

The images that are the subject of this paper are formed through a spectrograph via a reflection grating operated in first order. The reflection grating diffracts the incident light into its constituent wavelength components in a direction perpendicular to the grooves, as described by Eq. (1). If the spectrograph is operated with a narrow entrance slit (as would normally be the case for spectroscopic measurements), angle α is well defined and the light intensity on any position of the spectrograph exit plane is, via angle β and for Eq. (1), directly related to a specific wavelength λ. However, if the entrance slit is not narrow, angle α is not well defined, and this situation may give rise to ambiguity in the light-intensity distribution in the exit plane. In this broad-slit case, one dimension of the image (say, $\hat{x}$) in the exit plane contains both spatial and spectral information. The other dimension ($\hat{y}$; parallel to the grooves of the grating and to the height of the entrance slit) contains spatial information only and is omitted from the following discussion. Figure 2 depicts a cross section of the spectrograph, showing the entrance slit in the focal plane of a collimating lens, a reflective grating, and the exit port in the focal plane of a second lens. (In commercial spectrographs[16] mirrors are used instead of lenses, but this does not make a difference to the formalism presented.) The input image on the entrance slit is a real image, formed by an external lens (not shown in Fig. 2), of some (planar) light source. For clarity, Fig. 2 illustrates bichromatic light, in which the two wavelengths are chosen to be sufficiently distinct to prevent the two resultant images from overlapping. In practice, however, the incident light need not be bichromatic; it may be polychromatic, resulting in overlapping images.

In principle, all rays with a given wavelength λ

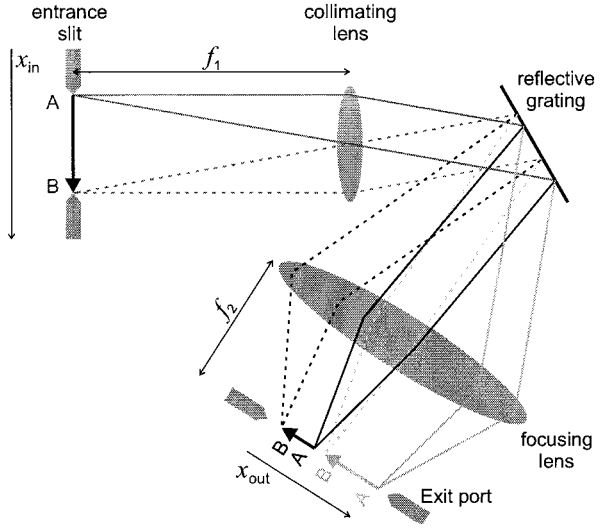

Fig. 2. Cross section of a spectrograph including a first-order ray trace for bichromatic light. The heights of the entrance slit and the exit port as well as the grooves of the grating are perpendicular to the plane of the picture. Also shown are coordinates x_{in} and x_{out} that appear in the formalism of Section 2.

originating from a specific point x_{in} in the entrance slit plane will be imaged onto exactly one point x_{out} in the exit plane, thus transforming spectral information into spatial information. Conversely, wavelength λ that can be associated with any position x_{out} in the exit plane also depends on source position x_{in}. For an extended, polychromatic source, therefore, the relation between λ and x_{out} is ambiguous. (This, in fact, is what usually is loosely referred to as loss of spectral resolution if the entrance slit of a spectrograph is broadened.) In general terms, the relation between measured light-intensity distribution T and incident intensity distribution S_{in} can be written as[17]

$$T(x_{out}) = \int_{\lambda} \int_{x_{in} \in slit} \mathcal{T}(\lambda, x_{in}; x_{out}) S_{in}(\lambda, x_{in}) d\lambda dx_{in}, \tag{2}$$

where $x_{in,out}$ are coordinates in the spectrograph entrance and exit planes, respectively, T is the (spatial) intensity distribution in the exit plane, S_{in} is the spectral and spatial intensity distribution in the entrance plane, and $\mathcal{T}$ is a transfer function. The integrations run over the whole spectrum and, according to the reasoning above, over the whole range of x_{in} along the width of the entrance slit. As there is input only at the entrance slit, the integration over space can be extended from $-\infty$ to $+\infty$ without affecting the result.[18]

For the present purpose, perfect imaging will be assumed, and only grating efficiency $\eta(\lambda)$ is accounted for. Under this assumption the transfer function links λ and x_{in} to x_{out} through the following equation:

$$\mathcal{T}(\lambda, x_{in}; x_{out}) = \eta(\lambda) \delta[x_{out} - f(\lambda, x_{in})], \tag{3}$$

in which the function $f(\lambda, x_{in})$ depends on grating diffraction and imaging optics. It is interpreted as the function that describes the place on the exit plane where a monochromatic point source, that has wavelength λ and is located at x_{in} would be imaged. The Dirac delta function allows only the signals of those combinations of λ and x_{in} for which a point x_{out} is illuminated to contribute to the signal at that point x_{out}.

Unraveling of the spectral and spatial information contained in the input pattern $S_{in}(\lambda, x_{in})$ requires that S_{in} can be factorized, that is, that

$$S_{in}(\lambda, x_{in}) = S_{\lambda}(\lambda) \times S(x_{in}). \tag{4}$$

This restriction, by the way, is not peculiar to OMA imaging but applies to spectrally selective imaging in general. It limits the interpretation of OMA graphs (that is, photographs taken through an OMA) to applications in which either the light source has a uniform spectral composition over the width of the entrance slit or the contributions from sources with different spatial and spectral distributions do not overlap on the OMA graph (see below, Subsection 3.A). In paper T2 we further discuss when and whether this factorization is justified for multispecies Raman scattered light. For the moment it suffices to assume that factorization holds for a single light source that has a spectral profile $S_{\lambda}(\lambda)$ and a spatial intensity distribution $S(x_{in})$. In this case the factorization leads to

$$\begin{aligned} T(x_{out}) &= \int_{\lambda} \int_{x_{in}} \eta(\lambda) \delta[x_{out} - f(\lambda, x_{in})] \\ &\quad \times S_{\lambda}(\lambda) S(x_{in}) d\lambda dx_{in} \\ &= \int_{x_{in}} \eta[\hat{f}(x_{in}; x_{out})] S_{\lambda}[\hat{f}(x_{in}; x_{out})] S(x_{in}) dx_{in}, \end{aligned} \tag{5}$$

where $\hat{f}(x_{in}; x_{out})$ is the inverse of $f(\lambda, x_{in})$, yielding λ given x_{in} and x_{out}. Note that $\hat{f}$ is a function of one variable (x_{in}) only, because x_{out} is a parameter dictated by the point under investigation.[19] In practice, angles α and β will vary only over small ranges. Linearization of the sines in the grating equation, Eq. (1) with a minus, then provides the relation among the three coordinates (subscripts 0 denote reference positions):

$$M_s(x_{in,0} - x_{in}) - (x_{out,0} - x_{out}) = \zeta\lambda. \tag{6}$$

This relation implies true imaging (magnification M_s, determined by the spectrograph) and linear diffraction (grating constant ζ, characterizing the grating). Both M_s and ζ are dimensionless quantities. The Dirac delta function in Eq. (3) selects $f(\lambda, x_{in}) = x_{out}$

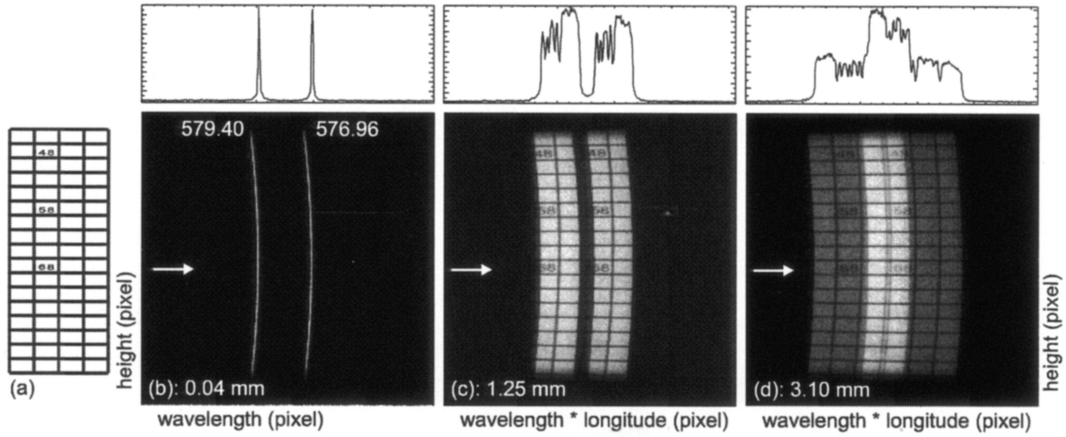

Fig. 3. Three OMA graphs recorded with different widths of the entrance slit of the spectrograph, as indicated in the photographs. The horizontal axes contain both spectral and spatial information, and the vertical axes are purely spatial. (a) Imaged object, a 5.0 mm × 5.0 mm grid printed on white paper with a linewidth of 0.5 mm; (b) spectrum of the light source [a Hg(Ar) calibration lamp; λ (in nanometers) indicated], recorded by reflection off white paper; (c), (d) OMA graphs of the object shown in (a) under illumination by the same source as in (b). The traces on top of the images are single-strip cross sections of the images at the positions of the arrows, cutting the lower circles of the "68" on the grid. All images are scaled individually. The curvature of the images and the horizontal extrusion of the grid are artifacts of the spectrograph.

from Eq. (6). For this simple relation the inverse function is cast explicitly as

$$\hat{f}(x_{\text{in}}; x_{\text{out}}) \equiv \lambda = \frac{(x_{\text{out}} - x_{\text{out},0}) - M_s(x_{\text{in}} - x_{\text{in},0})}{\zeta}. \quad (7)$$

Substitution of this specific inverse function results in $T(x_{\text{out}})$ of the form

$$T(x_{\text{out}}) = \int_{x_{\text{in}}} \eta\left[\frac{(x_{\text{out}} - x_{\text{out},0}) - M_s(x_{\text{in}} - x_{\text{in},0})}{\zeta}\right] \times S_\lambda\left[\frac{(x_{\text{out}} - x_{\text{out},0}) - M_s(x_{\text{in}} - x_{\text{in},0})}{\zeta}\right] \times S(x_{\text{in}})\mathrm{d}x_{\text{in}} \quad (8a)$$

$$= [(\eta \times S_\lambda) * S](x_{\text{out}}). \quad (8b)$$

This outcome represents a convolution (*) of a spectral distribution (that is shifted forward and compressed in its argument) with a spatial distribution.

As it is spatial pattern S that is of interest, it needs to be reconstructed from image T through a deconvolution procedure, once the spectral dependency ($\eta \times S_\lambda$) is known. One can obtain that dependency by recording $T(x_{\text{out}})$, using a narrow entrance slit (located at reference position $x_{\text{in},0}$ and illuminated with intensity S_0), in which case

$$S_\delta(x_{\text{in}}) = S_0\delta(x_{\text{in}} - x_{\text{in},0}), \quad (9)$$

where the subscript δ indicates the narrow entrance slit. For this input the convolution ends up as

$$T_\delta(x_{\text{out}}) = \eta\left[\frac{(x_{\text{out}} - x_{\text{out},0})}{\zeta}\right] S_\lambda\left[\frac{(x_{\text{out}} - x_{\text{out},0})}{\zeta}\right] S_0, \quad (10)$$

which, of course, is just a spectrum. As it is used to deconvolve an OMA graph for the spectral distribution, we refer to it as a spectral reference function, $R(x_{\text{out}})$, in what follows. To make the connection to Eqs. (8), we rewrite Eq. (10) as

$$\eta\left[\frac{(x_{\text{out}} - x_{\text{out},0}) - M_s(x_{\text{in}} - x_{\text{in},0})}{\zeta}\right] \times S_\lambda\left[\frac{(x_{\text{out}} - x_{\text{out},0}) - M_s(x_{\text{in}} - x_{\text{in},0})}{\zeta}\right] = \frac{R[x_{\text{out}} - M_s(x_{\text{in}} - x_{\text{in},0})]}{S_0}. \quad (11)$$

Backsubstitution of this expression for spectral reference function R turns the convolution, Eqs. (8), into its final form:

$$T(x_{\text{out}}) = \int_{x_{\text{in}}} R[x_{\text{out}} - M_s(x_{\text{in}} - x_{\text{in},0})]\,\frac{S(x_{\text{in}})}{S_0}\,\mathrm{d}x_{\text{in}}. \quad (12)$$

Note that grating efficiency η(λ) is canceled, because it is present in both spectral reference image R and convolved image S. Neither does grating constant ζ appear explicitly.

An example of the convolving action of the spectrograph is presented in Fig. 3, where three OMA graphs of a square grid under bichromatic illumination are shown for three entrance slit widths. Like all subsequent OMA graphs in this section, they were taken through an imaging spectrograph (Acton Research Corporation SpectraPro300i $f/4$ with a 2400-grooves/mm grating). The slight curvature of the OMA graphs is an imaging artifact of the spectrograph; it will be seen below that the deconvolution algorithm can automatically correct

for it. Also, the magnification of the spectrograph is 14% larger along the $\hat{x}$ direction than along the $\hat{y}$ direction, which causes the square grid to look rectangular; this anomaly not been corrected for in the examples presented here (but it was corrected for in companion paper T2). An intensified CCD camera (Princeton Instruments ICCD-512-T: 512×512 pixels; ∅25-mm intensifier; 16-bit dynamic range) at the exit port of the spectrograph recorded the OMA graphs corresponding to regions imaged by a camera objective (Nikon UV-Nikkor, 105 mm, $f/4.5$) on the entrance slit of the spectrograph. In the photographs of Fig. 3, slit width d_s is increased from 40 μm [Fig. 3(b)] to its maximum value of 3.10 mm [Fig. 3(d)]. The $d_s = 40$ μm OMA graph is taken as the infinitesimally narrow slit measurement of the spectral reference function for deconvolution purposes. It contains two lines of the mercury spectrum.[20] Further decrease of the entrance slit width did not result in a narrower line profile but only decreased the intensity levels. When the entrance slit is broadened, the spatial images produced by both lines broaden accordingly [Fig. 3(c)] and eventually overlap [Fig. 3(d)]. On top of every OMA graph the intensity along a single strip is plotted as a horizontal cross section (fixed y) at the height of the white arrows in the graphs.

The notion of recording a somehow distorted version of the original input image is not unfamiliar. In general imaging experiments, for example, artifacts are introduced by aberrations of the optical detection system and its limited resolution. In image-restoration literature[21–23] such artifacts are often described in terms of a point-spread function (psf), which describes how a point source is mapped onto the image plane by a convolution procedure that is similar to the one presented here. Although R is not exactly a psf, it can be thought of as acting as one by linking the input image to the output. Note, however, that R is not spatially invariant.

3. Deconvolution of Optical Multichannel Analyzer Graphs

The main result of Section 2 is an analytical expression, Eq. (12), for the intensity distribution in the exit plane of a spectrograph as a convolution of the spatial and spectral intensity distributions incident onto the entrance slit. In practice, one is often interested in just the spatial intensity distribution. In this section we focus on the deconvolution of the spectrograph output with the spectral distribution, which should provide the desired spatial input intensity distribution. Special attention is paid to the role of noise accumulated on the spectrograph output in the deconvolution procedure. First, a straightforward deconvolution algorithm is discussed and evaluated, followed by a more-sophisticated approach that yields much better results.

A. Analytical Formulation

The general formulation of the convolution as given in Eq. (12) forms the starting point for the deconvolution procedure and is here restated as

$$T(x_{\text{out}}) = \int_{x_{\text{in}}} R[x_{\text{out}} - M_s(x_{\text{in}} - x_{\text{in},0})]G(x_{\text{in}})\mathrm{d}x_{\text{in}} + \mathcal{N}(x_{\text{out}}), \tag{13}$$

where normalized pattern S/S_0 is replaced by G for notational convenience and a noise term $\mathcal{N}$ is added. The importance of this extra contribution to the formalism will become clear below. The reconstruction of original spatial distribution S requires a deconvolution of convolved image T (broad entrance slit measurement) with respect to spectral dependency R (narrow slit measurement). This inverse problem can be solved conveniently by Fourier transformation. The Fourier transform (FT) and its inverse are defined by

$$\mathrm{FT}[F(x)] \equiv \tilde{F}(k) \overset{\text{def}}{=} \int_x F(x)\exp(-ikx)\mathrm{d}x, \tag{14a}$$

$$\mathrm{FT}^{-1}[\tilde{F}(k)] \equiv F(x) \overset{\text{def}}{=} \frac{1}{2\pi}\int_k \tilde{F}(k)\exp(ikx)\mathrm{d}k, \tag{14b}$$

respectively. Application of the Fourier transform to the convolution, Eq. (13), yields

$$\tilde{T}(k) = \tilde{R}(k)\exp(iM_s k x_{\text{in},0})\tilde{G}(M_s k) + \tilde{\mathcal{N}}(k) \tag{15}$$

when one takes due care of magnification M_s and shift $x_{\text{in},0}$.[14] The convolution in direct space thus becomes a regular product in reciprocal (k) space, for which the components have decoupled.

Once the Fourier components $\tilde{T}(k)$ and $\tilde{R}(k)$ have been assessed, the Fourier components of the original image at the entrance slit can formally be obtained analytically by solution of Eq. (15) for $\tilde{G}$:

$$\tilde{G}(M_s k) = \frac{\tilde{T}(k) - \tilde{\mathcal{N}}(k)}{\tilde{R}(k)\exp(iM_s k x_{\text{in},0})}, \tag{16}$$

and after an inverse FT the entrance slit image in direct space, $G(x_{\text{in}})$, results.

In practical OMA imaging, the signal at the exit plane is recorded by a CCD camera, requiring a reformulation (discretization) of the analytical problem. Details of this procedure are given in Appendix A.

Figure 4 demonstrates the effect of the analytical deconvolution procedure [Appendix A, Eq. (A6)] to the data of Fig. 3. In this measurement there was noise in both the spectral reference signal [Fig. 3(b)] and the convolved distribution [Fig. 3(d)]. The straightforward deconvolution result is extremely noisy [Fig. 4(a)] and contains virtually no useful quantitative information, as can be seen clearly from the single-strip cross section above the image. Note that this occurs in spite of the fact that both input

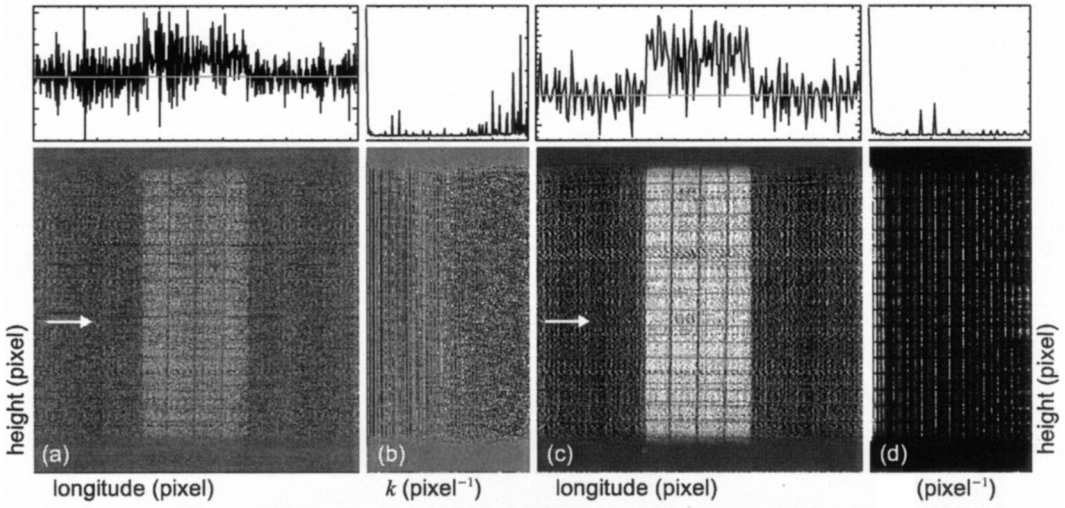

Fig. 4. Strip-by-strip deconvolution of Fig. 3(d) with the spectrum of Fig. 3(b) by means of the unfiltered Fourier-transformation algorithm [Eq. (A6) below]. Purely spatial images (a) and (c) show data in direct space; the corresponding power spectra are shown in (b) and (d) (first half of the k components only). (a), (b) Direct deconvolution; note the large high-k components in (b). (c), (d) Direct convolution but with two-pixel binning; the high-k components partly cancel (d). Top, single-strip cross sections at the positions of the arrows. [Zero baseline indicated in (a) and (c); left ordinates omitted in (b) and (d) to emphasize the low-k components.]

images [Figs. 3(b) and 3(d)] are not particularly noisy. A closer look at the reciprocal space components [Fig. 4(b)] indicates that the resultant noise can be attributed to large high-k components[24] that do not cancel each other on inverse Fourier transformation. The FT diagonalizes the convolution problem and hence the deconvolution. However, because many of its high-k components are small, the inverse problem is (numerically) ill conditioned and sensitive to small variations (noise) in the recorded data. In a more physical explanation, the deconvolution algorithm attempts to increase the contrast in the image; i.e., it attempts to restore structure in the input that was smeared out by the convolution: Any structure that is present in the measured (convolved) image must have been more pronounced in the actual spatial distribution on the entrance slit (before convolution). There is, however, no way for the reconstruction algorithm to distinguish real data from noise that is added during detection and superposes an artificial structure (on a pixel-to-pixel basis, that is, high-frequency) onto the convolved signal. As the analytical algorithm does not treat the noise any differently from the real data, it generates high-k components to account for the rapid pixel-to-pixel fluctuations in the measured (signal + noise) data. Unfortunately, it is not trivial to discriminate between real data and noise.

Zero padding the data (to array sizes up to 2^{13} pixels) to increase the resolution in k-space did not alter the deconvolved result in direct space significantly. Additional windowing of the raw data to impose periodic boundary conditions rigidly as required for the FT was also insufficient to restore the original image. This means that the noise in the straightforward reconstruction is not a consequence of ill-satisfied periodic boundary conditions. At the cost of losing spatial resolution, binning two neighboring pixels is a trivial low-pass filter for the spectral and the convolved data. A subsequent deconvolution yields Fig. 4(c), which looks less noisy than Fig. 4(a). Indeed, its corresponding Fourier power spectrum [Fig. 4(d)] shows fewer contributions from high-k components. However, although the structure of the object can now be recognized, the signal-to-noise ratio in Fig. 4(c) is still poor compared with the input [Fig. 3(d)]; compare especially the two single-strip cross sections above each image). Clearly, additional filtering is required for separation of data from noise by suppression of exploded $\tilde{G}(k)$ contributions, especially at higher reciprocal space components. There are filters that do this job globally,[22] but often they are *ad hoc* and do not provide dramatic improvements. A more general algorithm dedicated to filtered deconvolution is presented below.

B. Linear Bayesian Deconvolution Filter

The goal is to reconstruct the original spatial pattern $\{G_n\}$ (a strip of the input) that gave rise to a measurement $\{T_m\}$ (a strip of the output) for a given spectral convolution function $\{R_m\}$. As actual input $\{G_n\}$ is in principle unknown, many candidates might have given the same measured output (including noise), and one of these has to be selected. This boils down to finding the most likely reconstruction of $\{G_n\}$, given the incomplete knowledge provided by the experiment. "Incomplete" means that the actual noise contribution is not known, for example. What we do know, however, is (i) a measurement of the output and (ii) the convolution model of Eq. (12), which links the output to the input. A Bayesian statistical analysis[25] prescribes a procedure for quantifying the term "most likely" and for assigning reliability to the reconstruction. For this purpose the intensities of the input pattern, the measured data, and the noise are

thought of as stochastic variables to which pdf's that describe the probability that a stochastic variable will take a certain value. The spectral reference function is assumed to be well assessed as the response to a peak input. The principles of the data filter are presented in this paper; details can be found in the dissertation of Tolboom.[14]

In this section, uppercase letters denote stochastic variables and the corresponding lowercase letters represent their actual values (data). Boldface vector notation indicates that we deal with the entire set of N stochastic variables or their specific values; subscripts indicate a single component.

Given the pdf's and the experimental fact that the measurement of $\mathbf{T}$ resulted in the particular outcome $\mathbf{t}$ (denoted $\mathbf{T} = \mathbf{t}$), the reconstruction problem is equivalent to calculating the conditional expectation values

$$\mathbb{E}[\mathbf{G}|\mathbf{T} = \mathbf{t}] \equiv \mathcal{F}(\mathbf{t}) \tag{17}$$

as a function $\mathcal{F}$ of measured output $\mathbf{t}$. These conditional expectation values are the best *a posteriori* estimates of the *a priori* input $\mathbf{g}$, given the measured outcome $\mathbf{T} = \mathbf{t}$.[26] The criterion "best" is defined as that particular $\mathcal{F}(\mathbf{t})$ that minimizes the mean-square errors

$$\mathbb{E}[|G_n - \mathcal{F}_n(\mathbf{t})|^2] \ \forall_n, \tag{18}$$

based on the measured $\mathbf{T} = \mathbf{t}$. In this section we provide the best reconstruction by direct calculation of the conditional expectation value. It is Bayes's theorem, which is used to link *a priori* knowledge of both input and output to *a posteriori* knowledge. There are different ways to arrive at the final result, for example, by direct minimization of the mean-square error, either analytically or graphically.[14] However, we believe that the formulation presented below gives the clearest insight in the mathematics involved.

In the statistical approach, both input image $\mathbf{G}$ and noise $\mathcal{N}$ are modeled by stochastic variables, that is,

$$G_n = c + \sigma X_n \ \forall_n, \qquad \mathcal{N}_m = b + \tau Y_m \ \forall_m, \tag{19}$$

respectively, where the values of X_n and Y_m are taken *a priori* from mutually independent standard normal distributions, a choice that we comment on below. It is assumed in the model that all pixels in a strip are characterized by one set of parameters $\{c, \sigma, b, \tau\}$. The mutual independence (denoted $\perp\!\!\!\perp$) of all distributions $\mathbf{X}$ and $\mathbf{Y}$ implies that

$X_m \perp\!\!\!\perp X_n$ $(m \neq n)$, i.e., the pdf of the optics before the spectrograph is neglected;

$Y_m \perp\!\!\!\perp Y_n$ $(m \neq n)$, i.e., the noise is accounted for per individual pixel; and

$X_m \perp\!\!\!\perp Y_n \ \forall_{m,n}$, i.e., the noise is not correlated to the signal at all. (20)

As G (the normalized input signal) is a dimensionless quantity, parameters c and σ are dimensionless, too. b and τ have the same dimension as $\mathcal{N}$, however, which is [count]. It can be shown[14] that pdf $(\wp)$ of original image G_n taking on the value g_n can be derived from the standard normal distribution as

$$\wp_{G_n}(g_n) = \frac{1}{\sqrt{2\pi}\sigma} \exp\left[-\frac{1}{2}\left(\frac{g_n - c}{\sigma}\right)^2 \right] \ \forall_n \tag{21}$$

and similarly for the noise term

$$\wp_{\mathcal{N}_m}(\nu_m) = \frac{1}{\sqrt{2\pi}\tau} \exp\left[-\frac{1}{2}\left(\frac{\nu_m - b}{\tau}\right)^2 \right] \ \forall_m. \tag{22}$$

Parameters b and c are the averages of the noise and the normalized input image, respectively, and τ^2 and σ^2 are the variances in the corresponding signals. The distribution $\wp_{G_n}$ [Eq. (21)] illustrates the dilemma in choosing σ. On the one hand, σ has to be sufficiently large to include all the reasonable data, but on the other hand it should be small enough to exclude negative values (input g_m is necessarily positive), effectively by assigning small probabilities to them. The exclusion of negative numbers is not an issue for the noise model. The addition of mean c to the input is an extension to existing analytical models (such as those documented by MacKay[27]), because it shifts the *a priori* pdf to the (positive) intensities expected on physical principles. A physical approach to determining σ and τ is discussed at the end of this section.

The discretized form of the convolution model, Eq. (A2) below, provides the link between the assumed stochastic variables, Eqs. (19), and the output, which we can measure. These output values,

$$T_m = \sum_n R_{m-n+n_0} G_n + \mathcal{N}_m \ \forall_m, \tag{23}$$

are also treated as stochastic parameters in the current approach. Once the values $\mathbf{g} = (g_0, \ldots, g_{N-1})$ of input pattern $\mathbf{G} = (G_0, \ldots, G_{N-1})$ are specified, the pdf for the output follows from this equation as the conditional pdf (or likelihood):

$$\wp_{T_m}(t_m|\mathbf{G} = \mathbf{g}) = \frac{1}{\sqrt{2\pi}\tau} \times \exp\left\{ -\frac{1}{2}\left[\frac{t_m - \left(\sum_n R_{m-n+n_0} g_n + b \right)}{\tau} \right]^2 \right\} \ \forall_m. \tag{24}$$

This is an equation for a normal distribution once more, but it is now centered about the value $(\Sigma_n R_{m-n+n_0} g_n + b)$ with variance τ.

The problem in OMA imaging, however, is that we measure output $\mathbf{T} = \mathbf{t}$, from which we want to retrieve the pdf for the input pattern. This (*a posteriori*) pdf is also a conditional pdf, $\wp_{G_q}(g_q|\mathbf{T} = \mathbf{t})$, but it cannot be calculated readily. Fortunately, it suffices for our problem to calculate the conditional expecta-

tion value of G_q, which is defined for discrete stochastic variables as

$$\mathbb{E}[G_q|\mathbf{T}=\mathbf{t}] = \sum_{g_q} g_q \mathbb{P}[G_q = g_q|\mathbf{T}=\mathbf{t}] = \sum_{g} g_q \mathbb{P}[\mathbf{G}=\mathbf{g}|\mathbf{T}=\mathbf{t}]\ \forall_q. \quad (25)$$

(Note that each of these relations contains a summation over values g_q and $\mathbf{g}$ rather than a summation over components q. Inasmuch as the individual components are independent, this notation does not introduce additional components.[14]) Conditional probability $\mathbb{P}$ (of occurrence of an event; for discrete stochastic variables) that was introduced in Eq. (25) is related to conditional pdf $\wp$ (of a value; for continuous stochastic variables) by

$$\mathbb{P}[G_q \in (a, b)|\mathbf{T}=\mathbf{t}] = \int_a^b \wp_{G_q}(g_q|\mathbf{T}=\mathbf{t})\mathrm{d}_{g_q}. \quad (26)$$

It is at this point that Bayes's theorem

$$\mathbb{P}[\mathbf{G}=\mathbf{g}|\mathbf{T}=\mathbf{t}] = \frac{\mathbb{P}[\mathbf{T}=\mathbf{t}|\mathbf{G}=\mathbf{g}] \times \mathbb{P}[\mathbf{G}=\mathbf{g}]}{\mathbb{P}[\mathbf{T}=\mathbf{t}]} \quad (27)$$

enters the statistical approach to deconvolution by reversing the information ($\mathbf{T}=\mathbf{t}$) and the unknown ($\mathbf{G}=\mathbf{g}$) arguments of the likelihood, turning Eq. (25) into

$$\mathbb{E}[G_q|\mathbf{T}=\mathbf{t}] = \sum_{g} g_q \frac{\mathbb{P}[\mathbf{T}=\mathbf{t}|\mathbf{G}=\mathbf{g}] \times \mathbb{P}[\mathbf{G}=\mathbf{g}]}{\mathbb{P}[\mathbf{T}=\mathbf{t}]}\ \forall_q. \quad (28)$$

The denominator does not depend on $\mathbf{g}$, so it can be taken out of the sum. Additionally, the decomposition relation of probabilities is applied to the denominator:

$$\mathbb{P}[\mathbf{T}=\mathbf{t}] = \sum_{\mathbf{g}} \mathbb{P}[\mathbf{T}=\mathbf{t}|\mathbf{G}=\mathbf{g}] \times \mathbb{P}[\mathbf{G}=\mathbf{g}], \quad (29)$$

and the conditional expectation value becomes

$$\mathbb{E}[G_q|\mathbf{T}=\mathbf{t}] = \frac{\sum_{\mathbf{g}} g_q \mathbb{P}[\mathbf{T}=\mathbf{t}|\mathbf{G}=\mathbf{g}] \times \mathbb{P}[\mathbf{G}=\mathbf{g}]}{\sum_{g} \mathbb{P}[\mathbf{T}=\mathbf{t}|\mathbf{G}=\mathbf{g}] \times \mathbb{P}[\mathbf{G}=\mathbf{g}]}\ \forall_q, \quad (30)$$

showing that the numerator and the denominator contain the same probabilities and that the numerator carries the additional value g_q that is averaged. This is a relation that is familiar from statistical physics, for example, where the population of a grand canonical ensemble is normalized by the partition function.[28]

In the continuum limit of the stochastic variables, Eq. (30) contains Riemann summations that go over into integrals over pdf's for every pixel q:

$$\begin{aligned}
\mathbb{E}[G_q|\mathbf{T}=\mathbf{t}] &= \frac{\int_{\mathbb{R}^N} g_q \wp_{\mathbf{T}}(\mathbf{t}|\mathbf{G}=\mathbf{g}) \times \wp_{\mathbf{G}}(\mathbf{g})\mathrm{d}\mathbf{g}}{\int_{\mathbb{R}^N} \wp_{\mathbf{T}}(\mathbf{t}|\mathbf{G}=\mathbf{g}) \times \wp_{\mathbf{G}}(\mathbf{g})\mathrm{d}\mathbf{g}} \\
&= \frac{\int_{\mathbb{R}^N} g_q \exp\left[-\frac{1}{2}\left|\frac{\mathbf{t}-\mathbf{R}*\mathbf{g}-b}{\tau}\right|^2\right]\exp\left[-\frac{1}{2}\left|\frac{\mathbf{g}-c}{\sigma}\right|^2\right]\mathrm{d}\mathbf{g}}{\int_{\mathbb{R}^N} \exp\left[-\frac{1}{2}\left|\frac{\mathbf{t}-\mathbf{R}*\mathbf{g}-b}{\tau}\right|^2\right]\exp\left[-\frac{1}{2}\left|\frac{\mathbf{g}-c}{\sigma}\right|^2\right]\mathrm{d}\mathbf{g}} \\
&= \frac{\int_{\mathbb{R}^N} g_q \exp\left[-\frac{1}{2}\sum_m\left(\left|\frac{t_m-\sum_n R_{m-n+n_0}g_n-b}{\tau}\right|^2+\left|\frac{g_m-c}{\sigma}\right|^2\right)\right]\mathrm{d}\mathbf{g}}{\int_{\mathbb{R}^N} \exp\left[-\frac{1}{2}\sum_m\left(\left|\frac{t_m-\sum_n R_{m-n+n_0}g_n-b}{\tau}\right|^2+\left|\frac{g_m-c}{\sigma}\right|^2\right)\right]\mathrm{d}\mathbf{g}},
\end{aligned} \quad (31)$$

where all stochastic variables are independent and the prefactors in the numerator and the denominator cancel. Because the $\mathbf{g}$ and $\mathbf{R}$ values in the first part of the exponentials are coupled via the convolution, these integrals cannot be performed analytically in direct space. Substitution of the FTs of the $\mathbf{g}$, $\mathbf{R}$, $\mathbf{t}$, b, and c values provides a convenient change of the coordinates of integration that decouples the integrand once more. However, this change of coordinates is rather intricate and introduces some

complications with respect to the coordinates and domain of integration (see App. 6.A in the dissertation of Tolboom[14]). Analytical evaluation via reciprocal space of the integrals in Eq. (31) eventually leads to the key formula

$$\mathbb{E}[G_q|\mathbf{T}=\mathbf{t}] = \frac{c(\tau/\sigma)^2 - b\tilde{R}_{k=0}}{\tilde{R}_{k=0}^2 + (\tau/\sigma)^2} + \mathrm{FT}^{-1}\left[\frac{\tilde{R}_{k,n_0}^*\tilde{t}_k}{|\tilde{R}_{k,n_0}|^2 + (\tau/\sigma)^2}\right] \tag{32}$$

for the restoration of the unknown original input image. (A tilde denotes a FT; see Appendix A.)

Equation (32) is the main result of this paper, describing the reconstruction of the most probable input pattern by means of filtered deconvolution of the measured output. Because the expression is analytically closed, it enables straightforward implementation to be made in computer code without iterative loops. In Eq. (32) the first term denotes an offset about which data are scattered by FT^{-1} in the second term. Parameter c is always taken as the average over the convolved image $\mathbf{t}$.

The filter has only one free model parameter, fraction σ/τ, instead of two (σ and τ separately), as might perhaps be expected from the supposition of the stochastic variables of Eqs. (19). This effective filter parameter can be interpreted as a measure of the contrast between the real structure in the signal (e.g., the grid lines and the numbers) and the noise accumulated in the measurement.

Equation (32) is the linear Bayesian-filtered version of the straightforward deconvolution, Eq. (A6) below. To compare the two results we rearrange the argument of FT^{-1} in Eq. (32) according to

$$\frac{\tilde{R}_{k,n_0}^*\tilde{t}_k}{|\tilde{R}_{k,n_0}|^2 + (\tau/\sigma)^2} = \frac{|\tilde{R}_{k,n_0}|^2}{|\tilde{R}_{k,n_0}|^2 + (\tau/\sigma)^2}\frac{\tilde{t}_k}{\tilde{R}_{k,n_0}} = \frac{1}{1 + (\tau/\sigma)^2|\tilde{R}_{k,n_0}|^{-2}}\frac{\tilde{t}_k}{\tilde{R}_{k,n_0}}. \tag{33}$$

Equation (33) shows that the filter effectively suppresses all k components of the straightforward deconvolution by a factor $[1 + (\tau/\sigma)^2|\tilde{R}_{k,n_0}|^{-2}] \geq 1$. Alternatively, the power of the Fourier-transformed components within the inverse FT can be written as

$$\underbrace{\left|\frac{\tilde{R}_{k,n_0}^*}{|\tilde{R}_{k,n_0}|^2 + (\tau/\sigma)^2}\right|^2}_{\text{filtered deconvolution function}} = \underbrace{\left[\frac{|\tilde{R}_{k,n_0}|^2}{|\tilde{R}_{k,n_0}|^2 + (\tau/\sigma)^2}\right]^2}_{\text{filter}} \times \underbrace{\left|\frac{1}{\tilde{R}_{k,n_0}}\right|^2}_{\text{deconvolution function}}. \tag{34}$$

Written in this way, the Bayesian filter with the choice of normal distributions for the stochastic variables is seen to yield results similar to those of the Wiener deconvolution filter.[22]

The prefactor filter is a measure of the power attributed by the filter to the real data, depending only on spectral reference function R and regularization parameter σ/τ. It is clear that, if τ/σ approaches zero (i.e., the measured structures are completely due to structure in the input image), the nonfiltered deconvolution, Eq. (A6) below, will remain. In that limit, the offset in Eq. (32) approaches $-b/\tilde{R}_{k=0}$, corresponding to subtraction of (constant) noise level b from the deconvolved data. The results in this paper were obtained for $b = 0$, so there is no such additional offset correction for accumulated noise. The limit of $\tau/\sigma \to \infty$, however, would physically correspond to a measured output that is dominated by noise. In this case the filter effectively suppresses all Fourier components and results in the prediction of a flat input distribution.

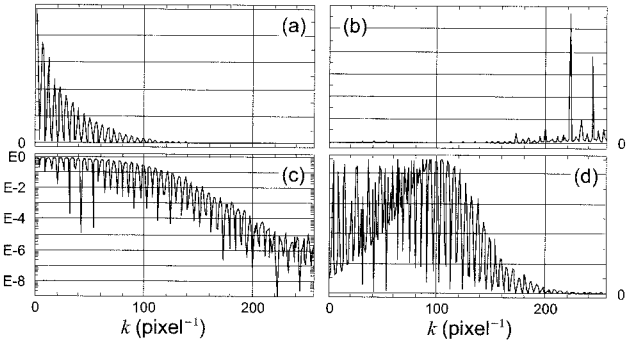

Fig. 5. Power spectra (single strips at the location of the arrows in Fig. 3). (a) Fourier-transformed spectral reference function $\tilde{R}_k$ of Fig. 3(b), (b) nonfiltered deconvolution function, (c) filtering of (b) (note the logarithmic scale), (d) linear Bayesian filtered deconvolution function. The power of the filtering function (c) is the prefactor *filter* of Eq. (34). (c), (d) Calculated for $\sigma/\tau = 6$ counts^{-1}.

Figure 5 illustrates the action of the (filtered) deconvolution in reciprocal space for the single-strip data $\tilde{\mathbf{R}}$ of Fig. 3(b). At the right in Fig. 5 are the powers of the deconvolution function [Fig. 3(b)] and of the filtered deconvolution function [Fig. 3(d)] on a linear scale. The spectrum in Fig. 3(b) is dominated by high-k components, and these cause extreme noise in the straightforward reconstruction [e.g., Fig. 4(a)]. As can be seen from Fig. 5(c), it is exactly these high-k components that are strongly suppressed by the filter factor, Eq. (34). As a result, the power spectrum of the filtered deconvolution [Fig. 5(d), which should be compared to Fig. 5(b)] is dominated by (real) structure in the low-k components, a structure that is present as only a minor wrinkle in the unfiltered spectrum [Fig. 5(b)]. The exact shape of the filter [Fig. 5(c)] strongly depends on the shape of $|\tilde{R}_k|^2$ [Fig. 5(a)]. In this case the presence of two spectral lines causes the oscillations in $|\tilde{R}_k|^2$, and in all traces derived from it. For a single-line spectrum, for example, all curves would have been smooth.

Figure 6 illustrates the dependence of the reconstruction on filter parameter σ/τ in more detail. The turning point for the filter's behavior, as can be seen from Eq. (34), lies at $\sigma/\tau \approx |R|^{-1}$. For $\sigma/\tau \lesssim |R|^{-1}$, the structure in the measured image is taken as dom-

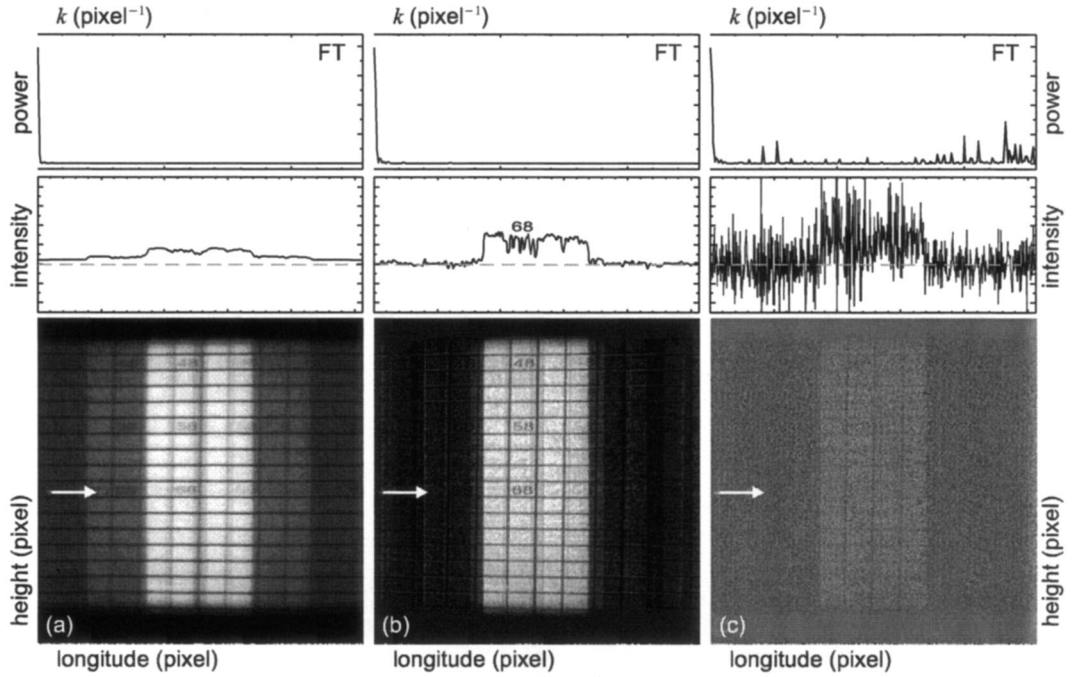

Fig. 6. Strip-by-strip linear Bayesian deconvolution of Fig. 3(d) with the spectrum of Fig. 3(b). Right to left, results for three ratios σ/τ, ranging from (a) too low ($\sigma/\tau = 1$ count^{-1}) to (b) best ($\sigma/\tau = 6$ counts^{-1}) to (c) too high ($\sigma/\tau = 800$ counts^{-1}). Above the images are the single-strip cross sections (similar to those in Figs. 3 and 4), and on top of them are their power spectra for the first halves of k components. The images are scaled individually, but the traces are all on the same linear gray scale. The left ordinates of the power spectra are omitted to show the similarity of the barely filtered, low-k components.

inated by noise, whereas for $\sigma/\tau \gtrsim |R|^{-1}$ it is attributed to the input image itself. The former situation results in a relatively uniform input image [as reflected in the smooth reconstruction of Fig. 6(a)] onto which readout noise has imposed structure. The latter situation corresponds to an input image with rich structure onto which relatively little noise has accumulated. The deconvolution therefore produces a wildly fluctuating image [Fig. 6(c)] approaching the nonfiltered deconvolution result. In the best result (here $\sigma/\tau = 6$ counts^{-1}; see below), the original object is well reproduced, and the other parts of the image are nearly empty. (Ideally, they would be completely dark.) The horizontal cross sections (white arrows similar to those in Figs. 3 and 4) emphasize the accurate recovery of the input image; three distinct minima represent the grid lines in the single-strip data, and an intermediate structure is present that comes from cutting the "68". The grid minima are separated by approximately 43 pixels, and they are somewhat broader than 4 pixels (full width at half-maximum), in perfect agreement with the printed grid of 1:10 for the line thickness. Still, there are a few small undershoots (oscillations and negative numbers), also in the best result. As discussed after the Eqs. (21) and (22) for the pdf's, their presence does not come as a surprise.

Although rigorous mathematical procedures exist for estimating regularization parameter σ/τ (see, e.g., Engl *et al.*[29]), we have opted for a more physical approach. The physical situation is that light is transmitted through the entrance slit only. Thus after deconvolution the signal should ideally be confined to a finite area on the CCD chip that corresponds to the entrance slit image, while the rest of the chip is empty. Define the image contrast as $\langle P(\text{in})\rangle/\langle P(\text{out})\rangle$, with $\langle P(\text{in})\rangle$ the average power inside the reconstructed entrance slit image (pixel numbers 176–335) and $\langle P(\text{out})\rangle$ the average power outside this part of the image (pixel numbers 1–165). The best σ/τ should then maximize the image contrast. From a plot of the image contrast compared with σ/τ (Fig. 7), such is found to be the case for $\sigma/\tau = 6$ counts^{-1}. Note that the maximum in Fig. 7 is rather broad, so the filter's performance is not critical to the exact value of σ/τ that is used.

A final check on the quality of the reconstructed image lies in reconvolving it with the spectral refer-

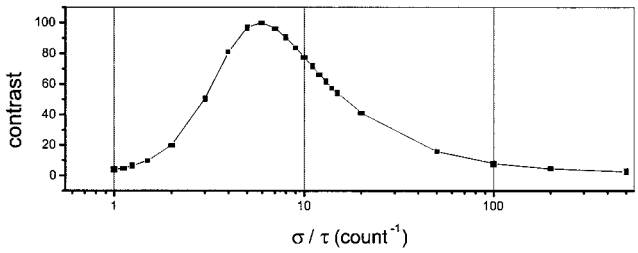

Fig. 7. Contrast (defined in the text) as a function of σ/τ. The maximum in the curve is taken as the best σ/τ for the deconvolution as it minimizes the relative power in the physically dark region. The corresponding value for the nonfiltered results [Fig. 4(a)] is $\langle P(\text{in})\rangle/\langle P(\text{out})\rangle = 1.35$.

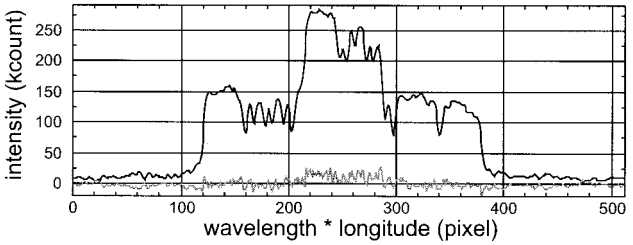

Fig. 8. Reconvolved image of the data that were obtained with a deconvolution for $\sigma/\tau = 6$ counts^{-1} (solid curve) and its difference from the original, measured data (residual; gray curve). The difference is 0.04 count on average and has a standard deviation of more than 7 kcounts.

ence function, as was done for Fig. 8. The difference of this result from the measured data is also indicated; it is 1–2 orders of magnitude smaller than the actual data. The average power in the reconvolved image is 0.946 times the average power contained in the original data, so the filter attributes approximately 5% of the power to noise for $\sigma/\tau = 6$ counts^{-1}.

4. Some Properties of Optical Multichannel Analyzer Imaging and the Reconstruction of Optical Multichannel Analyzer Graphs

A. Linearity

The linearity of the deconvolution filter can be demonstrated by consideration of the deconvolution of any linear combination of two measurements $\mathbf{T} = (a_1\mathbf{t}_1 + a_2\mathbf{t}_2)$ given by

$$\begin{aligned}\mathbb{E}[G_q|\mathbf{T} = a_1\mathbf{t}_1 + a_2\mathbf{t}_2] &= (a_1 + a_2)\,\frac{c(\tau/\sigma)^2 - b\tilde{R}_{k=0}}{\tilde{R}_{k=0}^2 + (\tau/\sigma)^2} \\ &\quad + \mathrm{FT}^{-1}\left[\frac{\tilde{R}^*_{k,n_0}\{a_1 t_{1k} + a_2 t_{2k}\}}{|\tilde{R}_{k,n_0}|^2 + (\tau/\sigma)^2}\right] \\ &= a_1\mathbb{E}[G_q|\mathbf{T} = \mathbf{t}_1] + a_2\mathbb{E}[G_q|\mathbf{T} = \mathbf{t}_2]. \qquad (35)\end{aligned}$$

The factor $(a_1 + a_2)$ before the offset term may not be obvious. As the total signal now consists of two separate measurements (t_1 and t_2) multiplied by the factors a_1 and a_2, the average value c and the average noise level b of the two images need to be multiplied by the same factor. Note that the linearity is a consequence of our specific choice of standard normal distributions in Eqs. (19) rather than of its being presupposed in the derivation of Eq. (32). The physical implication for OMA imaging is that (spectral) structures that do not overlap in an OMA graph can be treated separately. Thus various sources with different spectral distributions can be recorded in a single OMA graph as long as their contributions do not overlap in the exit plane. [See Fig. 3(c); the deconvolved image can be found in Tolboom's dissertation.[14]] Thus the factorization requirement stated in Eq. (4) is seen not to be any more severe for OMA imaging than for any other kind of spectrally selective imaging.

B. Two-Dimensional Image Reconstruction

A spectrograph, like any other optical device, introduces imaging defects. Because the effects of these defects increase with distance from the optical axis, nondiffracting dimension $\hat{y}$ in particular will suffer from defects. The imaging artifacts of the system used in our experiments can be judged from Fig. 3(a). The two spectral lines (images of a straight entrance slit) are curved, and they become a bit less sharp toward the upper and lower ends. Both effects do not noticeably vary over the width of the image. As horizontal cross sections are treated individually, the perfect-imaging assumption of Eq. (3) is fulfilled for each strip. Furthermore, the strip-by-strip deconvolution provides two additional advantages related to the inherent properties of deconvolution. If the spectral reference function is recorded with the same spectrograph settings as the image [but with a narrow entrance slit, of course; cf. Figs. 3(a) and 3(c)], the reference image will contain a spectral reference function on each image line (pixel row). The deconvolution (i) will take into account the one-dimensional psf as part of the spectral reference function and (ii) will center the deconvolved image about the origin.[30] Thus, if individual strips of an OMA graph are deconvolved with a spectral reference function of the corresponding strip in a spectral reference image [like that of Fig. 4(a)], both the additional blurring and the curvature are corrected for. In some practically complicated cases, the spectral reference function cannot be determined for every strip or need to be averaged for a sufficient signal-to-noise ratio. In such cases the reconstruction will still contain residual blurring, the curvature will persist, or both. Nevertheless, these images can often be used in quantitative studies, as shown in companion paper T2.

C. Improvements and Restrictions

A main advantage of the Bayesian deconvolution filter presented here is that it is expressed in closed form [Eq. (32)]. Thus the expectation values can be calculated directly, which obviates the need for CPU-intensive optimization schemes. This direct calculation, however, has its price. We had to assume linear imaging [Eq. (6)] and found that the linearity of the filter in fact arises from our choice of normally distributed stochastic variables [Eq. (19)]. The linear imaging assumption was required for the spectrograph output to take on the form of a convolution [Eq. (12)]. It may break down for extended spectral structures, depending also on the equipment used. Probably the best check of whether this assumption is justified will be empirical.

The choice of normal distributions for the stochastic variables is in itself not expected to be a serious restriction, but it does allow (unphysical) negative values to appear in the final result (see the discussion of Fig. 6 above). More-elaborate distributions could remedy this defect but probably at the expense of not yielding a closed expression for the filter any more.

Such, for example, is the case with the maximum entropy method,[31] for which positivity of the reconstruction is ensured but finding it requires a numerical global optimization algorithm.

Finally, there is the assumption of (piecewise) factorizability of the input [Eq. (4)]. We do not consider this a restriction that is peculiar to OMA imaging but rather one that holds for all spectrally selective quantitative imaging schemes. In fact, we consider it one of the advantages of using a spectrograph compared, for instance, with bandpass filters: If the factorizability assumption breaks down, the spectrum will at least tell you that it does.

5. Summary and Conclusions

Under the hypothesis of factorizability of the input to a linearized spectrograph into a purely spectral and a purely spatial part, the entangling of spatial and spectral information by an optical multichannel analyzer setup is described effectively by a convolution. Reconstruction is achieved by a dedicated linear Bayesian deconvolution filter, depending on one free model parameter only. The data filter is based on Gaussian probability-density functions for the unknown spatial input and the accumulated noise, allowing for a closed analytical filter expression [Eq. (32)]. The resultant reconstruction shows clear contrast and a good reproduction of the factual input. Moreover, the algorithm prescribes a recipe for generating quantitatively interpretable data, thus satisfying an essential criterion for quantitative two-dimensional imaging.

Inasmuch as OMA imaging requires just an imaging spectrograph and a single camera, it is a reliable, relatively cheap, efficient technique for quantitative imaging experiments. A practical application is discussed in the companion paper.[15]

Appendix A. Discretization

The photodetection chip in a CCD camera[32] has a finite (say, N) number of pixels of finite (nonzero) dimension. These properties require a discretization of the analytical formulation [Eq. (13)]. As the pixels have a finite dimension, they already integrate the signal over a finite region of x_{out}. All integrals over space therefore become a sum over the subintegrals, i.e., the pixel values. The discretized version of Eq. (13) thus reads as

$$T_{n_{\text{out}}} = \sum_{n_{\text{in}}} R_{n_{\text{out}}-M_s(n_{\text{in}}+n_{\text{in},0})} \times G_{n_{\text{in}}} + \mathcal{N}_{n_{\text{out}}}, \quad \text{(A1)}$$

where n_{out} and n_{in} denote discrete positions (or, equivalently, pixel numbers) and replace continuous parameters x_{out} and x_{in}, respectively. This discretization implies that not only the output signal at the exit port but also the input signal at the entrance slit is discretized. Thus the aim will be to estimate signal G as a function of pixel number (discretized position). The subscript $[n_{\text{out}} - M_s(n_{\text{in}} + n_{\text{in},0})]$ of spectral reference function R labels the (discretized) wavelength. It is expressed in terms of both discrete positions n_{in} and n_{out} and need not be an integer because it contains the magnification $M_s \in \mathbb{R}$. From Eq. (6), however, we know that for every wavelength λ any specific $M_s n_{\text{in}}$ (or $M_s x_{\text{in}}$) may be converted into a specific n_{out} (or x_{out}), where n_{in} and n_{out} both denote pixel numbers. Therefore the references to "in" and "out" can be omitted and the subscripts can simply be any integer counter without reference to the specific planes (input or output).

Another consequence of the CCD chip's having only a finite number of pixels is that T and R can be recorded only for a finite number of points. The experimental settings must, of course, be such that this finite segment is representative of the complete signal so this representative part can be put into the convolution. When periodic boundary conditions (period N) are assumed, the discretized convolution in direct space [Eq. (A1)] becomes

$$T_m = \sum_{n=0}^{N-1} R_{m-n+n_0} \times G_n + \mathcal{N}_m. \quad \text{(A2)}$$

All subsequent summations and products over indices will be from 0 through $N - 1$.

The discretized form of the Fourier transform and its inverse are[33]

$$\tilde{F}_k = \sum_{n=0}^{N-1} F_n \exp\left(-\frac{2\pi i k n}{N}\right),$$
$$F_n = \frac{1}{N} \sum_{k=0}^{N-1} \tilde{F}_k \exp\left(\frac{2\pi i k n}{N}\right), \quad \text{(A3)}$$

respectively. Like m and n, k is merely a counter, which denotes the reciprocal space component of a Fourier-transformed signal. The discrete FTs are implemented in a computer program as fast FTs on 512 ($=2^9$) data points. The discretized analog of Eq. (15) is

$$\tilde{T}_k = \tilde{R}_{k,n_0} \times \tilde{G}_k + \tilde{\mathcal{N}}_k, \qquad \tilde{R}_{k,n_0} \overset{\text{def}}{=} \tilde{R}_k \exp\left(\frac{2\pi i k n_0}{N}\right), \quad \text{(A4)}$$

and the relation for the discretized deconvolved signal in reciprocal space [Eq. (16)] becomes

$$\tilde{G}_k = \frac{\tilde{T}_k - \tilde{\mathcal{N}}_k}{\tilde{R}_{k,n_0}}. \quad \text{(A5)}$$

As phase factor $\exp(2\pi i k n_0/N)$ will always appear in combination with $\tilde{R}_k$, it is absorbed by the latter for notational brevity, as is indicated by the additional subscript n_0 to $\tilde{R}_{k,n_0}$. The pixel values in direct space are

$$G_n = \text{FT}^{-1}[\tilde{G}_k] = \text{FT}^{-1}\left[\frac{\tilde{T}_k - \tilde{\mathcal{N}}_k}{\tilde{R}_{k,n_0}}\right]$$
$$= \frac{1}{N} \sum_{k=0}^{N-1} \left[\frac{\tilde{T}_k - \tilde{\mathcal{N}}_k}{\tilde{R}_{k,n_0}}\right] \exp\left(\frac{2\pi i k n}{N}\right), \quad \text{(A6)}$$

where the subscript n numbers the pixels (formally in the entrance slit plane). Because the Fourier algorithm is essentially just a mathematical trick, the physical information should be contained only in the real part of FT^{-1}. The imaginary part ought to vanish. The program that performed the deconvolution, Eq. (A6), was tested successfully on computer-generated data (not shown). The average power[34] in the imaginary part was always found to be ~25 orders of magnitude smaller than the average power in the real part, and indeed zero within the limit of computational accuracy.

We appreciate the critical and constructive discussions that we had with Marianna Sijtsema. This study was made possible by financial support from the Technology Foundation, the Applied Science Division of the Netherlands Organisation for Scientific Research, and the technology program of the Ministry of Economic Affairs.

References and Notes

1. A. C. Eckbreth, *Laser Diagnostics for Combustion Temperature and Species*, 2nd ed. (Gordon & Breach, Amsterdam, 1996).
2. K. Kohse-Höinghaus and J. B. Jeffries, *Applied Combustion Diagnostics* (Taylor & Francis, New York, 2002).
3. W. Merzkirch, *Flow Visualization* (Academic, Orlando, Fla., 1987).
4. W. Demtröder, *Laser Spectroscopy—Basic Concepts and Instrumentation*, 2nd ed., Vol. 5 of Springer Series in Chemical Physics (Springer-Verlag, Berlin, 1996).
5. E. Hecht, *Optics*, 4th ed. (Addison-Wesley, San Francisco, Calif., 2002).
6. S. P. Nandula, T. M. Brown, P. A. Skaggs, R. W. Pitz, and P. A. DeBarber, "Multi-species line Raman measurements in H_2-air turbulent flames," paper AIAA-94-0227, presented at the 32nd AIAA Aerospace Sciences Meeting, Reno, Nev., 10–13 January, 1994 (American Institute for Aeronautics and Astronautics, Reston, Va., 1994).
7. M. Mansour and Y. Chen, "Line Raman, Rayleigh, and laser-induced predissociation fluorescence technique for combustion with a tunable KrF excimer laser," Appl. Opt. **35,** 4252–4260 (1996).
8. F. Rabenstein and A. Leipertz, "One-dimensional, time-resolved Raman measurements in a sooting flame made with 355-nm excitation," Appl. Opt. **37,** 4937–4943 (1998).
9. G. Grünefeld, H. Schlüter, and P. Andresen, "Simultaneous multiple-line Rayleigh–Raman/LIF measurements in combustion," Appl. Phys. B **70,** 309–313 (2000).
10. J. O. Gilmore, S. Sharma, D. Fletcher, and D. Bershader, "Single-pulse spontaneous Raman scattering measurements in an expanding nitrogen/oxygen admixture," paper AIAA-95-2125, presented at the 30th AIAA Thermophysics Conference, San Diego, Calif., 19–22 June, 1995 (American Institute for Aeronautics and Astronautics, Reston, Va., 1995).
11. G. Tejeda, J. M. Fernández-Sánchez, and S. Montero, "High-performance dual Raman spectrometer," Appl. Spectrosc. **51,** 265–276 (1997).
12. N. M. Sijtsema, R. A. L. Tolboom, N. J. Dam, and J. J. ter Meulen, "Two-dimensional multispecies imaging of a supersonic nozzle flow," Opt. Lett. **24,** 664–666 (1999).
13. R. A. L. Tolboom, N. J. Dam, N. M. Sijtsema, and J. J. ter Meulen, "Quantitative spectrally resolved imaging through a spectrograph," Opt. Lett. **28,** 2046–2048 (2003).
14. R. Tolboom, "Expanding laser diagnostics in non-seeded compressible flow research," Ph.D. dissertation (University of Nijmegen, Nijmegen, The Netherlands, 2002), available from http://webdoc.ubn.kun.nl/mono/t/tolboom_r/expaladii.pdf.
15. R. A. L. Tolboom, N. J. Dam, and J. J. ter Meulen, "Quantitative imaging through a spectrograph. 2. Stoichiometry mapping by Raman scattering," Appl. Opt. **43,** 5682–5690 (2004).
16. A. Thorne, U. Litzén, and S. Johansson, *Spectrophysics: Principles and Applications* (Springer-Verlag, Berlin, 1999).
17. R. A. L. Tolboom, N. M. Sijtsema, N. J. Dam, and J. J. ter Meulen, "Raman imaging for combustion diagnostics," paper AIAA-00-0956, presented at the 38th AIAA Aerospace Sciences Meeting, Reno, Nev., 14–19 January, 2000 (American Institute for Aeronautics and Astronautics, Reston, Va., 2000).
18. Unless explicitly stated otherwise, the integration limits will be from $-\infty$ to $+\infty$ for (reciprocal) space coordinates and from 0 to $+\infty$ for wavelengths and frequencies.
19. Compare this to rolling two dice, λ and x_{in}, the sum of their results being x_{out}. There are various combinations of (λ, x_{in}) that lead, for example, to $x_{out} = 7$. These combinations are described by $f(\lambda, x_{in})$. Once outcome x_{out} is chosen to be 7, however, there is only one corresponding λ for every x_{in}, namely, $\hat{f}(x_{in}; x_{out})$.
20. The line at $\lambda = 579.40$ nm is an unresolved doublet. In fact, the exact wavelengths used do not matter for the processing of OMA graphs.
21. R. C. Gonzalez and R. E. Woods, *Digital Image Processing* (Prentice-Hall, Upper Saddle River, N.J., 2002).
22. K. C. Castleman, *Digital Image Processing* (Prentice-Hall, Englewood Cliffs, N.J., 1996).
23. H. C. Andrews and B. R. Hunt, *Digital Image Restoration* (Prentice-Hall, Englewood Cliffs, N.J., 1977).
24. As input signal $S(x)$ of the FT is purely real, the Fourier-transformed data $\tilde{S}(k)$ are even under complex conjugation; i.e., $\tilde{S}(-k) = \tilde{S}^*(k)$. Therefore, only the positive k components need to be plotted to represent all power information.
25. See, e.g., P. M. Lee, *Bayesian Statistics: An Introduction*, 2nd ed. (Arnold, London, 1997).
26. R. Durrett, *Probability: Theory and Examples* (Duxbury, Belmont, Calif., 1991).
27. D. J. C. MacKay, "Information theory, inference, and learning algorithms," draft 2.4.1, 2002, available from http://www.inference.phy.cam.ac.uk/itprnn/book.pdf.
28. M. Plischke and B. Bergersen, *Equilibrium Statistical Physics*, 2nd ed. (World Scientific, Singapore, 1994).
29. H. W. Engl, M. Hanke, and A. Neubauer, *Regularization of Inverse Problems* (Kluwer Academic, Dordrecht, The Netherlands, 1996).
30. This is a general property of Fourier transformation. For visual clarity, the reconstructions presented in this paper (Figs. 4 and 6) have been recentered in the image frames.
31. B. Buck and V. A. Macaulay, *Maximum Entropy in Action* (Clarendon, Oxford, 1991).
32. See, e.g., Ref. 1, Sec. 3.6.
33. W. H. Press, S. A. Teukolsky, W. T. Vetterling, and B. P. Flannery, *Numerical Recipes in C—The Art of Scientific Computation*, 2nd ed. (Cambridge U. Press, Cambridge, Mass., 1992).
34. In this paper the convention is that the power or the absolute square of a signal S is defined as the signal times its complex conjugate (i.e., $|S|^2 = S \times S^*$), and the norm of the signal $\|S\|$ is the integral over S.